

## KSP-SN-2016kf: A LONG-RISING H-RICH TYPE II SUPERNOVA WITH UNUSUALLY HIGH <sup>56</sup>Ni MASS DISCOVERED IN THE KMTNET SUPERNOVA PROGRAM

NILOUFAR AFSARIARDCHI\*,<sup>1</sup> DAE-SIK MOON,<sup>1</sup> MARIA R. DROUT,<sup>1,2,3</sup> SANTIAGO GONZÁLEZ-GAITÁN,<sup>4</sup> YUAN QI NI,<sup>1</sup>  
CHRISTOPHER D. MATZNER,<sup>1</sup> SANG CHUL KIM,<sup>5,6</sup> YOUNGDAE LEE,<sup>5</sup> HONG SOO PARK,<sup>5</sup> AVISHAY GAL-YAM,<sup>7</sup> GIULIANO PIGNATA,<sup>8,9</sup>  
BON-CHUL KOO,<sup>10</sup> STUART RYDER,<sup>11</sup> SANG-MOK CHA,<sup>5,12</sup> AND YONGSEOK LEE<sup>5,12</sup>

<sup>1</sup>*Department of Astronomy and Astrophysics, 50 St. George St., Toronto, ON M5S 3H4, Canada, University of Toronto*

<sup>2</sup>*Hubble Fellow, Carnegie Observatories, 813 Santa Barbara Street, Pasadena, California, 91101 USA*

<sup>3</sup>*Dunlap Institute, University of Toronto, Toronto, ON M5S 3H4, Canada*

<sup>4</sup>*CENTRA, Instituto Superior Técnico, Universidade de Lisboa, Av. Rovisco Pais 1, 1049-001 Lisboa, Portugal*

<sup>5</sup>*Korea Astronomy and Space Science Institute, 776 Daedeokdae-ro, Yuseong-gu, Daejeon 34055, Republic of Korea*

<sup>6</sup>*Korea University of Science and Technology, Daejeon 34113, Republic of Korea*

<sup>7</sup>*Department of Particle Physics and Astrophysics, Weizmann Institute of Science, Rehovot, Israel, 76100*

<sup>8</sup>*Departamento de Ciencias Físicas - Universidad Andres Bello, Avda. Republica 252, Santiago, 8320000 Chile*

<sup>9</sup>*Millennium Institute of Astrophysics (MAS), Nuncio Monsenor Sotero Sanz 100, Providencia, Santiago, Chile*

<sup>10</sup>*Department of Physics and Astronomy, Seoul National University, Seoul 151-747, Republic of Korea*

<sup>11</sup>*Department of Physics and Astronomy, Macquarie University, NSW 2109, Australia*

<sup>12</sup>*School of Space Research, Kyunghee University, 1732 Deogyong-daero, Giheung-gu, Yongin-si, Gyeonggi-do, 17104, Republic of Korea*

### Abstract

We present the discovery and the photometric and spectroscopic study of H-rich Type II supernova (SN) KSP-SN-2016kf (SN2017it) observed in the KMTNet Supernova Program in the outskirts of a small irregular galaxy at  $z \approx 0.043$  within a day from the explosion. Our high-cadence, multi-color ( $BVI$ ) light curves of the SN show that it has a very long rise time ( $t_{\text{rise}} \approx 20$  days in  $V$  band), a moderately luminous peak ( $M_V \approx -17.6$  mag), a notably luminous and flat plateau ( $M_V \approx -17.4$  mag and decay slope  $s \approx 0.53$  mag per 100 days), and an exceptionally bright radioactive tail. Using the color-dependent bolometric correction to the light curves, we estimate the <sup>56</sup>Ni mass powering the observed radioactive tail to be  $0.10 \pm 0.01 M_{\odot}$ , making it a H-rich Type II SN with one of the largest <sup>56</sup>Ni masses observed to date. The results of our hydrodynamic simulations of the light curves constrain the mass and radius of the progenitor at the explosion to be  $\sim 15 M_{\odot}$  (evolved from a star with an initial mass of  $\sim 18.8 M_{\odot}$ ) and  $\sim 1040 R_{\odot}$ , respectively, with the SN explosion energy of  $\sim 1.3 \times 10^{51}$  erg  $\text{s}^{-1}$ . The above-average mass of the KSP-SN-2016kf progenitor, together with its low metallicity  $Z/Z_{\odot} \approx 0.1 - 0.4$  obtained from spectroscopic analysis, is indicative of a link between the explosion of high-mass red supergiants and their low-metallicity environment. The early part of the observed light curves shows the presence of excess emission above what is predicted in model calculations, suggesting there is interaction between the ejecta and circumstellar material. We further discuss the implications of the high progenitor initial mass and low-metallicity environment of KSP-SN-2016kf on our understanding of the origin of Type II SNe.

*Key words:* supernovae: general – supernovae: individual (KSP-SN-2016kf)

Online-only material: color figures

arXiv:1906.09271v1 [astro-ph.HE] 21 Jun 2019

## 1. INTRODUCTION

Massive stars ( $M_{\text{ZAMS}} \gtrsim 8 M_{\odot}$ ) end their lives with the collapse of their core, leading to supernova (SN) explosions in most cases. Type II SNe are those core-collapse SNe (CC-SNe) whose progenitor retain part of their H envelope until the explosion. Some H-rich Type II SNe are marked with light curves featured with a distinctive post-peak plateau of  $\sim 100$  days. Following the often-undetected shock breakout (SBO) after the explosion, the envelope of the progenitor radiates shock-deposited energy (Nakar & Sari 2010; Rabinak & Waxman 2011). After a few days, as the recombination front moves inside the ejecta, the H recombination emission becomes the dominant emission powering the plateau (Popov 1993). This plateau emission is supplemented by contributions from the radioactive decay of  $^{56}\text{Ni}$ , depending on the  $^{56}\text{Ni}$  mixing level within the envelope (Nakar et al. 2016). Later, the energy released by the radioactive decay of  $^{56}\text{Ni}$  becomes the primary power source and the light curves enter the phase of the radioactive tail, followed by an optically thin nebular phase in a few months. Here, we avoid further classifying H-rich Type II SNe into traditional Type IIP and IIL sub-types due to increasing evidence that the transition between two classes is continuous (e.g., Arcavi 2017, and references therein).

Although red supergiants (RSGs) are largely considered to be the progenitor of H-rich Type II SNe, there still remains the critical uncertainty about the mass range of their progenitors. The RSGs identified in pre-explosion images of H-rich Type II SNe appear to have initial masses smaller than  $\sim 17 M_{\odot}$ , which is significantly lower than the upper limit of  $\sim 25 M_{\odot}$  typically predicted in theories (Smartt 2015) as well as the observed RSGs in the Milky Way and Magellanic clouds (Levesque et al. 2005, 2006). It has been argued that this discrepancy, called the ‘Red supergiant problem’ (Smartt et al. 2009), may originate from unaccounted extinction in the circumstellar dust (Walmswell & Eldridge 2012) or inaccurate bolometric correction (Davies & Beasor 2018). However, the origin of the lack of the observationally identified Type II progenitors in the mass range of  $15\text{--}25 M_{\odot}$  remains still unknown. There also exist theoretical uncertainties about the fate of massive stars, whose initial masses are in the range of  $\gtrsim 17 M_{\odot}$ , and how they explode as SNe due largely to incomplete understanding of rotation, mixing, and mass-loss processes as well as binary effect. It may be possible that at least some RSGs in this mass range with a significant mass-loss rate have their envelopes stripped, leading to more compact progenitors and, consequently, non-Type II SNe such as Type Ib/c or Iib, although what fraction of the RSGs can have such drastically substantial mass-loss rates is poorly understood (van Loon et al. 2005; Smith 2014). In addition, even the origins of the non-Type II – i.e., Type Iib and Ib/c – SNe are also somewhat uncertain

considering the lack of observational samples of progenitors of those SNe whose initial masses are  $\gtrsim 20 M_{\odot}$  (e.g., Drout et al. 2011; Lyman et al. 2016) and the uncertainty of whether some of them originate from single stripped-envelope stars (e.g., Wolf-Rayet stars) or binary stars (Smartt 2009). Interestingly, several recent studies suggest that massive RSGs in this mass range may rather produce a failed SN and implode to a black hole (O’Connor & Ott 2013; Sukhbold et al. 2016) as potentially exemplified by the disappearance of a  $25 M_{\odot}$  RSG in a nearby galaxy NGC 6946 (Adams et al. 2017), rendering the mapping between the progenitor masses and their final fates quite challenging. We note, however, that metallicity may be an important factor determining how the massive RSGs explode as SNe. This is because most of the H-rich Type II SNe observed with a smaller, i.e.,  $\lesssim 17 M_{\odot}$ , progenitor mass have been found in a host galaxy with a relatively high metallicity greater than  $0.5 Z_{\odot}$ , while Anderson et al. (2018) reported the detection of a low-metallicity, i.e.,  $0.1 Z_{\odot}$ , H-rich Type II SN whose initial progenitor mass is thought to be in the range of  $17\text{--}25 M_{\odot}$ . This is suggestive that the RSGs whose initial masses are in the range of  $\gtrsim 17 M_{\odot}$  may prefer low-metallicity environments for them to explode as Type II SNe, and it is imperative to increase the observational sample in order to support, or disapprove this tantalizing possibility.

Another important uncertainty in our understanding of the Type II SNe is the amount of  $^{56}\text{Ni}$  masses produced in the explosion. Statistical analyses based on the observed properties of the large number of recently-discovered Type II SNe have shown that they have a significant diversity in the observational characteristics such as rise time, peak brightness, decline rate, expansion velocity, and tail luminosity (Arcavi et al. 2012; Anderson et al. 2014; Sanders et al. 2015; González-Gaitán et al. 2015; Rubin et al. 2016; Valenti et al. 2016). The mass of  $^{56}\text{Ni}$  produced in Type II SN explosions obtained from the analysis of their tail luminosities is considerably larger than what is predicted by neutrino-driven CCSN simulations (Ugliano et al. 2012; Pejcha & Thompson 2015; Sukhbold et al. 2016), suggesting that our understanding of how Type II SNe explode is incomplete. The identification and detailed observational studies of Type II SNe with a large  $^{56}\text{Ni}$  mass, therefore, can provide valuable insights into their progenitors and explosion mechanisms.

It is worthwhile to note that the observational studies of SNe, including H-rich Type II, often rely on insufficiently-sampled light curves without early coverage and color information. However, early rise time light curves contain vital information on key progenitor parameters, especially progenitor radius (e.g., Rubin et al. 2016; Rubin & Gal-Yam 2017). Furthermore, the small number of SNe observed with early light curves make it difficult to investigate important processes involved in the explosions, including potential

interactions with a binary companion (Kasen 2010), aspherical behaviours (Afsariardchi & Matzner 2018) as well as mass-loss history of progenitors prior to the explosion (e.g., Yaron et al. 2017, and references therein).

Indeed, the growing number of early SN detections have shown strong indications for the presence of the circumstellar material (CSM) at the vicinity of their progenitors, including excess emission in the early light curve compared to the predictions of SBO cooling emission model (Morozova et al. 2018; Forster et al. 2018) as well as “flash-ionized” narrow H or He emission lines in the early spectra that disappear within hours or days following the explosion (Gal-Yam et al. 2014; Khazov et al. 2016; Yaron et al. 2017; Bullivant et al. 2018; Hosseinzadeh et al. 2018). These facts suggest that the progenitors of these SNe may have undergone a short period of enhanced pre-SN mass loss or outbursts in the final years leading to core collapse. The nature of this dense CSM is still unclear, but one promising mechanism that can lead to its formation is pre-SN wave heating outbursts (Quataert & Shiode 2012; Fuller 2017; Ro & Matzner 2017; Fuller & Ro 2018). High-cadence early observations of SNe are crucial for constraining the structure of such CSM and shining light on the types of SNe experiencing enhanced pre-SN mass loss.

In this paper, we present the discovery and observational studies, supplemented by numerical simulation work, of a H-rich Type II SN KSP-SN-2016kf that we detected at a very early epoch, likely within  $\sim 1$  day from the explosion, using the high-cadence, multi-color data obtained in the KMTNet (Korea Microlensing Telescope Network) Supernova Program (Moon et al. 2016). Our multi-color ( $BVI$ ) coverage from the early epoch allows us to model the early light curves and precisely measure the explosion epoch and the rise time of the light curves, leading to important insights into its progenitor, especially the progenitor radius and potential CSM characteristics.

This paper is organized as follows. In §2 we describe the discovery and photometric and spectroscopic observations of KSP-SN-2016kf, which is followed by light curve analysis and the estimation of  $^{56}\text{Ni}$  mass in §3. §4 and §5 provides the spectroscopic analysis of the SN and its host, respectively, whereas §6 does the hydrodynamic simulations for the progenitor and potential interaction with the CSM. We discuss the implications of our results for understanding the Type II SNe in §7, and conclude in §8.

## 2. OBSERVATIONS AND DISCOVERY

### 2.1. Photometry and Discovery

KSP-SN-2016kf (SN2017it<sup>1</sup>) was first detected on December 24, 2016 as part of the KMTNet Supernova Program (KSP; Moon et al. 2016). The KMTNet is a network of three 1.6 m telescopes located in Chile, South Africa, and Australia, providing 24-hour continuous sky coverage. Each telescope of the KMTNet is equipped with a wide field CCD camera covering  $2^\circ \times 2^\circ$  field at  $0''.4$  pixel sampling (Kim et al. 2016). The KSP conducts high-cadence  $BVI$  monitoring of a sample of fields focusing on studying early supernovae and rapidly evolving transients (e.g., He et al. 2016; Antoniadis et al. 2017; Park et al. 2017; Lee et al. 2018; Brown et al. 2018). Between 2016 October and 2017 May, we obtained about 600 images per each  $BVI$  band, with a mean cadence of roughly 9 hours per band, for a field around the nearby galaxy NGC 2188. All the images were obtained with 60-s exposure time, reaching  $\sim 20.5$ – $22.5$  limiting magnitudes<sup>2</sup> depending on the filter and observational conditions.

Figure 1 shows  $B$ -band images of a field containing KSP-SN-2016kf, including (a) a deep stack image of a  $\sim 4' \times 4'$  field around the source, (b) the last image before the detection of KSP-SN-2016kf at MJD=57745.488, (c) the first detection image of KSP-SN-2016kf at MJD=57746.867 and (d) around peak brightness at MJD=57759.146. As in Figure 1(b), KSP-SN-2016kf was first captured in the  $B$ -band with magnitude of  $\sim 20.4$  at (R.A., decl.) (J2000) = (06<sup>h</sup>10<sup>m</sup>37.156<sup>s</sup>,  $-34^\circ 08' 28''.3$ ) in the outskirts of an elongated faint irregular galaxy  $\sim 4''$  (or  $\sim 3.6$  kpc at the angular diameter distance of 181.5 Mpc, see below §2.3 for the measurement of distance to the galaxy) away in the western direction. See §5 for the identification of the galaxy as the host galaxy of KSP-SN-2016kf based on spectroscopic information.

The KSP real-time data processing pipeline first performs the bias subtraction, cross talk removal, and flat-fielding of the science images. Next, the astrometric solution is obtained by SCAMP<sup>3</sup> (Bertin 2006) using  $\sim 10000$  unsaturated stars which have a counterpart in the second Hubble guide star catalogue (Lasker et al. 2008), resulting in precision of  $\sim 0''.12$ .

For the KSP-SN-2016kf, we subtracted from the science images reference images made from pre-SN images of the field using the HOTPANTS<sup>4</sup> program (Becker 2015). Since the SN is close to its host galaxy, image subtraction is crucial for reducing the effect of the host galaxy on the SN pho-

<sup>1</sup> <https://wis-tns.weizmann.ac.il/object/2017it>. Note that although the first detection of KSP-SN-2016kf was made in 2016 by the KMTNet as we report in this paper, the official registration of the source in the Transient Name Server as an astronomical transient was made by Gaia Alerts team based on its detection of the source on January 5, 2017.

<sup>2</sup> All magnitudes are reported in Vega system.

<sup>3</sup> <http://www.astromatic.net/software/scamp>

<sup>4</sup> <http://www.astro.washington.edu/users/becker/v2.0/hotpants.html>

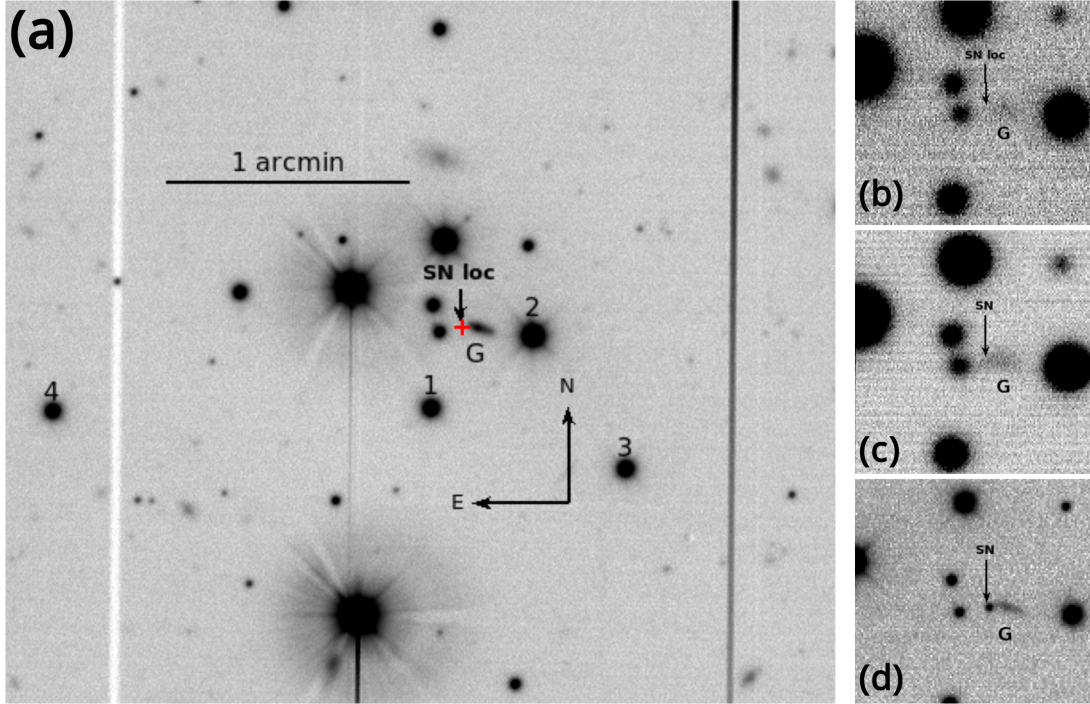


**Figure 1.** *B*-band images of KSP-SN-2016kf field. (a) A deep stacked image of the field made from 114 high quality images from 2016 October until 2016 December before the SN explosion. The host galaxy of KSP-SN-2016kf is indicated by letter “G” and the SN position is identified by a red cross. The numbered stars are a few of the standard stars used for photometric calibration. On the right panel, the evolution of KSP-SN-2016kf is shown in *B*-band at different epochs including (b) the last non-detection at MJD=57745.488, (c) the first detection at MJD=57746.867, and (d) around maximum brightness at MJD=57759.146.

tometry. By adjusting HOTPANTS parameters, we ensured that the subtraction is done efficiently and does not introduce bias in the subtracted science images. The photometry was then carried out on subtracted science images using our custom-developed software that performs PSF fitting and obtains the photometric solution based on  $\sim 35$  AAVSO All-Sky Survey nearby standard stars<sup>5</sup>. The photometry of KSP-SN-2016kf before applying any corrections is provided in Table 1.

## 2.2. Spectroscopy

We obtained a spectrum of KSP-SN-2016kf on March 27, 2017, which is 93 days after the first detection, using the WFCCD spectrograph mounted on the 2.5-m du Pont telescope at Las Campanas Observatory. The spectrum was acquired with the low resolution “blue” grism and a  $1''.65$  slit aligned with the parallactic angle, providing a wavelength coverage of  $\sim 3500\text{--}9000\text{ \AA}$ .

Bias and flat field correction, sky subtraction, spectral extraction, and wavelength calibration were performed us-

**Table 1.** KSP-SN-2016kf optical photometry

Time [MJD]	Filter	Magnitude <sup>1</sup> [mag]	Error [mag]
57745.488	<i>B</i>	>21.01	-
57745.489	<i>V</i>	>21.04	-
57745.490	<i>I</i>	>20.62	-
57746.867	<i>B</i>	20.56	0.14
57746.868	<i>V</i>	20.41	0.15
57746.869	<i>I</i>	20.36	0.23
57747.482	<i>B</i>	19.98	0.09
57747.483	<i>V</i>	19.96	0.09
57747.485	<i>I</i>	20.06	0.18
57747.867	<i>B</i>	19.74	0.04
57747.869	<i>V</i>	19.64	0.05
57747.870	<i>I</i>	19.68	0.08

<sup>1</sup> Magnitudes are in Vega system and not corrected for extinction.

NOTE—Table 1 is published in its entirety in the electronic edition. A portion is shown here for guidance regarding its formatting.

<sup>5</sup> <https://www.aavso.org/apass>

ing standard tasks in IRAF<sup>6</sup> (Tody 1993). In addition to the spectrum of KSP-SN-2016kf we also extracted a spectrum of the host galaxy from the same data. Flux calibration and telluric correction of both spectra were performed using a set of custom IDL scripts (see, e.g., Matheson et al. 2008; Blondin et al. 2012). The observation of standard stars for flux calibration was made after the SN observation on the same night. The observed spectra and the results of our spectroscopic analysis are presented in §4.

### 2.3. Redshifts, Reddening Correction and $K$ -Corrections

We measure the redshift of the host galaxy of KSP-SN-2016kf to be  $0.043 \pm 0.002$  using the  $H\alpha$  line in the host galaxy spectrum. The value is consistent with the redshift measured with the SN spectrum, confirming that the irregular galaxy G (Figure 1) is the host galaxy of KSP-SN-2016kf (see § 4 and 5 for the details of the spectroscopic analysis and the redshift measurements). In this paper we adopt the standard  $\Lambda$ CDM cosmology with Hubble constant  $H_0 = 67.4 \text{ km s}^{-1} \text{ Mpc}^{-1}$ , matter density parameter  $\Omega_M = 0.315$ , and vacuum density parameter  $\Omega_\Lambda = 0.685$  (Planck Collaboration et al. 2018). The luminosity distance and the distance modulus of the host galaxy based on these parameters are 197.4 Mpc and 36.48 mag, respectively. Table 2 contains a list of the key parameters of KSP-SN-2016kf obtained in our analysis.

Since KSP-SN-2016kf is located in the outskirts of the host galaxy, it is highly unlikely that there exists any substantial host galaxy extinction. We, therefore, only consider the extinction from the Milky Way in our reddening correction. This is supported by the absence of the Na ID  $\lambda\lambda 5890, 5896$  doublet absorption feature, which is known to be indicative of host galaxy extinction (e.g. Poznanski et al. 2012), in our SN spectrum (see §4). Our extinction measurement using the observed Balmer Decrement also shows that the host galaxy extinction is negligible (see §5 for the details). We obtain the Galactic extinction  $E(B - V) \approx 0.029$  mag toward the location of KSP-SN-2016kf using the extinction model of Schlafly & Finkbeiner (2011) and conduct a reddening correction of the extinction assuming  $A_V/E(B - V) = 3.1$ .

In addition to the reddening correction, we also carry out  $K$ -corrections to obtain the final photometric solution using the default  $(1+z)$   $K$ -Correction factor (Oke & Sandage 1968). Note that we ignore the effect of the SED shape on the  $K$ -corrections as our photometric solution based on the SN spectrum indicates the effect is negligible at the redshift of KSP-SN-2016kf. We also ignore the time dilation effect given its low redshift.

<sup>6</sup> IRAF is distributed by the National Optical Astronomy Observatory, which is operated by the Association for Research in Astronomy, Inc. under cooperative agreement with the National Science Foundation.

**Table 2.** KSP-SN-2016kf parameters

Parameter	Value
Redshift, $z$	$0.043 \pm 0.002$
Reddening <sup>1</sup> , $E(B - V)$ [mag]	$0.029 \pm 0.001$
Shock breakout time, $t_{\text{SBO}}$ [MJD]	$57746.74 \pm 0.07$
Offset from host galaxy, $r$ [kpc]	$3.4 \pm 0.2$
Luminosity distance, $d_L$ [Mpc]	$197.4 \pm 10.9$
Angular diameter distance, $d_A$ [Mpc]	$181.5 \pm 9.3$
Distance modulus, $\mu$ [mag]	$36.48 \pm 0.12$
$^{56}\text{Ni}$ mass, $M_{\text{Ni}} [M_\odot]$	$0.10 \pm 0.01$

<sup>1</sup> Galactic dust extinction from Schlafly & Finkbeiner (2011)

## 3. LIGHT CURVE ANALYSIS

### 3.1. Light Curve Evolution

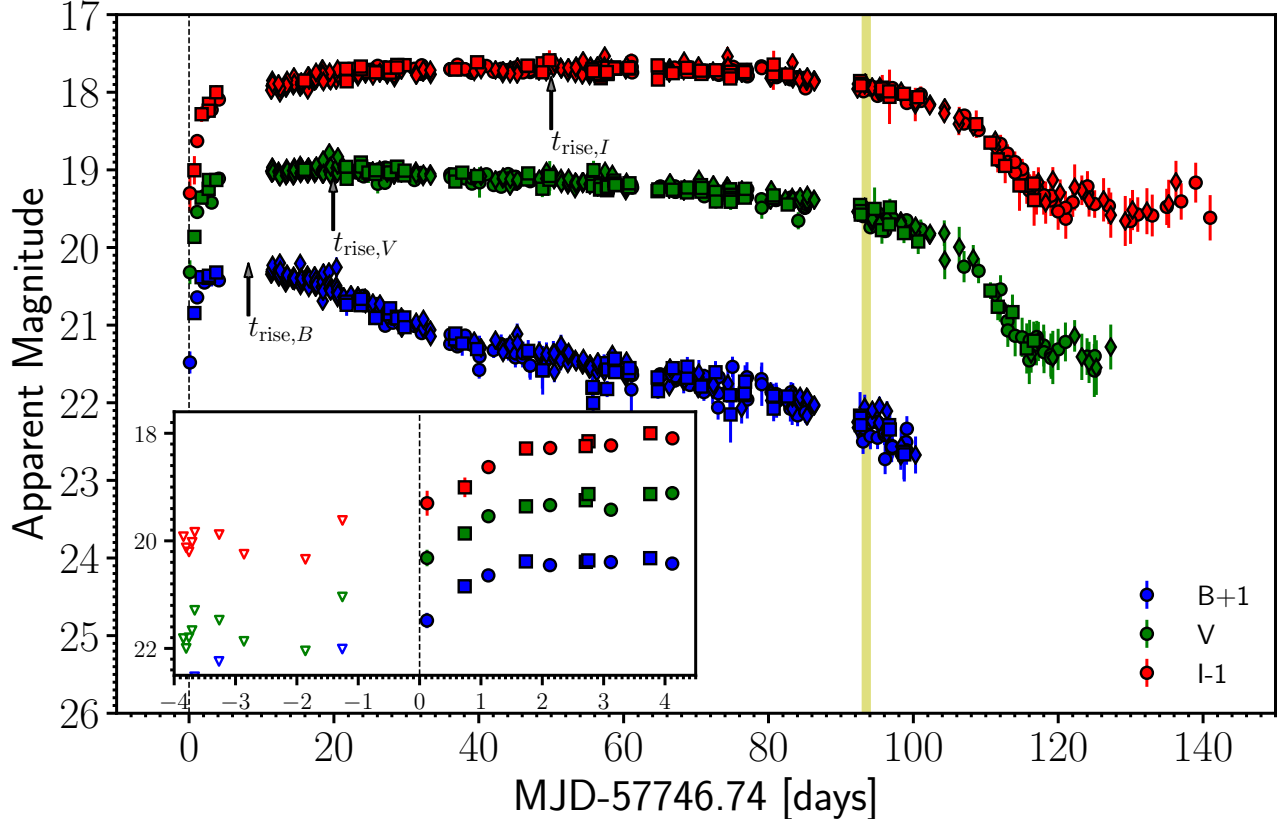
As explained above, KSP-SN-2016kf was first detected on December 24, 2016, MJD = 57746.867 in the  $B$  band with  $20.56 \pm 0.14$  mag followed by detections in the  $V$  and  $I$  bands, 2 and 4 minutes later, respectively, with  $20.41 \pm 0.15$  ( $V$ ) and  $20.36 \pm 0.23$  ( $I$ ) mag. The last  $BVI$  non-detection images were obtained  $\sim 33$  hours before the first detections with limiting magnitudes of  $\sim 21.01$  ( $B$ ),  $\sim 21.04$  ( $V$ ),  $\sim 20.62$  ( $I$ ) mag at the  $3\text{-}\sigma$  confidence level.

Figure 2 provides the entire light curves that we obtained for KSP-SN-2016kf with KMTNet, spanning over 140 days. As can be seen in Figure 2, the  $V$ -band light curve of KSP-SN-2016kf rises for  $\sim 20$  days (see below for the precise rise time measurement) before entering a plateau phase of  $\sim 105$  days during which the light curve slowly declines. Over the interval of  $\sim 90$ – $110$  days from the SBO, the light curves dim for  $\sim 1.5$  mag and transition into a slowly-decaying tail. The described light curve evolution and, in particular, the prominent plateau phase of KSP-SN-2016kf, together with the timescales of its distinctive phases of evolution, identify this transient as a H-rich Type II SN (Type IIP SN, Arcavi et al. 2012). Note that the SN nature is also confirmed by the spectroscopic information presented in §4.

In order to obtain the epoch of first light of KSP-SN-2016kf, which is the SBO epoch for CCSNe (Matzner & McKee 1999), we fit the early part of the light curves by the following equation

$$N_\lambda = \begin{cases} C_\lambda (t - t_0)^n & t > t_0 \\ 0 & t \leq t_0 \end{cases}, \quad (1)$$

where  $N_\lambda$  is normalized flux by its peak value in each band,  $t$  time measured from the epoch of the first detection,  $t_0$  the epoch of SBO relative to the epoch of the first detec-



**Figure 2.** Light curves of KSP-SN-2016kf in  $BVI$  bands, vertically shifted for readability. The x-axis represents time since our estimated  $t_{\text{SBO}} = 57746.74$ . The filled circle, diamond, and square markers indicate the observations made by South African, Chilean, and Australian telescopes, respectively. The open inverted triangles in the zoomed-in version of the early light curve mark non detection upper limits. The yellow line represents the spectroscopy epoch and the dashed line is our estimated SBO time. The rise times in  $BVI$  are marked by vertical arrows. Note that the light curves are corrected for Milky Way extinction  $E(B - V) = 0.029$  mag (from Schlafly & Finkbeiner 2011).

tion,  $n$  power index, and  $C_\lambda$  fitting coefficient. We only consider the epochs within 5 days from the first detection as well as upper limits for the epochs of non-detections in the fitting procedure. We fit the  $BVI$  light curves of KSP-SN-2016kf simultaneously and find the following best-fit parameters:  $t_0 = -0.12 \pm 0.07$  days,  $(C_B, C_V, C_I) = (0.69 \pm 0.04, 0.63 \pm 0.03, 0.39 \pm 0.02)$ , and  $n = 0.32 \pm 0.04$ . Figure 3 compares the best fit power laws with the observed  $BVI$  early light curves, where the SBO epoch  $t_0 = -0.12$  days is marked with vertical dotted line. In calendar days, this SBO epoch corresponds to  $t_{\text{SBO}} = 57746.74 \pm 0.07$  MJD (i.e., December 24, 2016).

For measuring the rise time of KSP-SN-2016kf, we use two methods: 1)  $t_{\text{rise}}$  is the time from  $t_{\text{SBO}}$  to the maximum light  $t_{\text{peak}}$  found by fitting a low order polynomial to the observed light curves; 2)  $t_{\text{baz}}$  is defined as the time from  $t_{\text{SBO}}$  to the maximum of the Bazin et al. (2009) exponential functional form fitted to the observed light curves. Table 3 summarizes the best-fit  $t_{\text{rise}}$  and  $t_{\text{baz}}$ . We found that  $t_{\text{baz}}$  is smaller than

$t_{\text{rise}}$  for KSP-SN-2016kf. The difference between the two times is notable for  $I$  band, for which the early light curve exhibits two distinct slopes over 50 days: an initial steep rise during the first  $\sim 20$  days and a slow rise to the peak during which the magnitude changes only  $\sim 0.3$  mag over  $\sim 30$  days. Note that  $t_{\text{baz}}$  tends to represent the time scale of the former slope (González-Gaitán et al. 2015) and therefore it is particularly shorter than  $t_{\text{rise}}$  in the  $I$  band. In Table 3, the high uncertainty in the  $B$ -band  $t_{\text{rise}}$  is due to the lack of data between  $\sim 4$  and  $\sim 10$  days post-discovery.

After the rise, the light curves reach the peak magnitude  $M_{\text{peak}} \simeq -17.40$  ( $B$ ),  $-17.62$  ( $V$ ), and  $-17.92$  ( $I$ ) mag, followed by the plateau phase. During the plateau phase, the light curves decay slowly, especially in the  $V$  and  $I$  bands. We measure the plateau length of  $\sim 105$  days by fitting a Fermi-Dirac function to the transition part of the light curves (Valenti et al. 2016). Table 3 contains the  $BVI$  decay rates of the light curves during the plateau phase. Between the epoch of  $\sim 90$  and  $\sim 118$  days, the light curves rapidly

**Table 3.** Light Curve Parameters of KSP-SN-2016kf

	<i>B</i>	<i>V</i>	<i>I</i>
Rise Time, $t_{\text{rise}}$ [days]	$8.2 \pm 3.6$	$19.9 \pm 1.2$	$50.0 \pm 1.2$
Bazin <sup>1</sup> Rise Time, $t_{\text{baz}}$ [days]	$7.93 \pm 4.51$	$10.78 \pm 6.62$	$31.22 \pm 10.72$
Peak Absolute Magnitude, $M_{\text{peak}}$ [mag]	$-17.40 \pm 0.16$	$-17.62 \pm 0.14$	$-17.92 \pm 0.13$
Absolute Magnitude at 50 days, $M_{50}$ [mag]	$-16.34 \pm 0.15$	$-17.47 \pm 0.14$	$-17.92 \pm 0.13$
Decay Rate, $s$ [mag/100 days]	$1.37 \pm 0.07$	$0.53 \pm 0.04$	$0.02 \pm 0.01$
Tail Absolute Magnitude, $M_{\text{tail}}$ [mag]	–	$-15.40 \pm 0.15$	$-16.30 \pm 0.15$

NOTE—The quantities are measured with respect to the epoch of first light at 57746.74 MJD.

<sup>1</sup> Obtained by fitting a functional form proposed in Bazin et al. (2009)

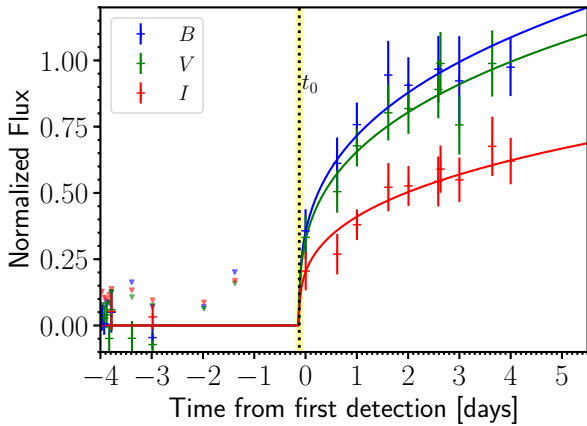


**Figure 3.** Estimated epoch of SBO. We fit a power law to the fluxes normalized to their corresponding peak values in *B* (blue curve), *V* (green curve), and *I* (red curve) bands. We only consider the epochs with fluxes within 5 days of the first detection including upper limits of non-detection epochs for fitting the epoch of first light. We mark the best fitted epoch of first light  $t_0 \approx -0.12$  days with dotted vertical line, while its  $1-\sigma$  confidence level of 0.07 days is shown with yellow strip. The non-detection limiting fluxes are shown with inverted triangles.

decline by more than 2 mag in the *V* and *I*, after which they settle into a radioactive tail, lasting for an extended period of time with a slow, gradual dimming.

### 3.2. Light Curve Comparison

Figure 4 compares the light curves of KSP-SN-2016kf with those of eight other Type II SNe in *BVI* band – all of them are of H-rich Type II, except for SN1987A classified as Type II-Peculiar. The epochs are relative to *B*-band peak brightness for each SN; except for SN1987A, which are relative to the first *B*-band detection due to its double-peaked light curve shape. We can identify in Figure 4 that there exists a significant diversity among Type II SNe in their luminosities and decay rates. KSP-SN-2016kf has highest luminosity of

the other SNe shown: in particular, both its plateau and tail luminosities are higher. Furthermore, the decay rate of KSP-SN-2016kf is among the smallest which makes the plateau look nearly flat in the *I* band. In terms of the shape of the light curves, KSP-SN-2016kf resembles those of SN2014cx, SN1999em, and LSQ13dpa but is notably more luminous. The *I*-band light curve of KSP-SN-2016kf has a peculiar bell shape, which has been also observed for SN2014cx.

Comparing the rise time of KSP-SN-2016kf to the rise time distribution of González-Gaitán et al. (2015), we find that the *V*- and *I*-Band rise times of KSP-SN-2016kf are, respectively, more than  $1-\sigma$  and  $2-\sigma$  above the median of  $t_{\text{rise}}$ —i.e., 11.5 (*V*) and 19.3 (*I*) days. Likewise,  $t_{\text{baz}}$  of KSP-SN-2016kf in *I* band is more than  $3-\sigma$  above than the median of Type II SNe, while in *B* and *V* bands, the  $t_{\text{baz}}$  is within  $1-\sigma$  of the median. Based on this high value of  $t_{\text{rise}}$ , KSP-SN-2016kf can be considered a “long riser” Type II SN in the definition of Taddia et al. (2016a).

Additionally, the plateau of KSP-SN-2016kf at 50 days is among the most luminous ones observed with absolute magnitude  $M_V \approx -17.47$  mag, while its peak magnitude is only moderately bright at  $M_V \approx -17.62$  mag. This highlights that the decay rate of KSP-SN-2016kf is relatively small. The decay rates of Type II SNe are often characterized by two slopes: an initial steep slope that immediately follows the light curve peak and a smaller decay rate that precedes the end of the plateau (Anderson et al. 2014). However, as Valenti et al. (2016) highlights, not all H-rich Type II SNe exhibit distinct slopes during the plateau phase. Indeed, KSP-SN-2016kf—similar to SN2014cx and prototypical SN1999em—shows nearly constant decay at the rate  $s \approx 0.53$  mag per 100 days in *V* band in the interval 30–70 days.

The decay rate and peak magnitude of Type II SNe are strongly correlated (Sanders et al. 2015). We test whether KSP-SN-2016kf also follows this correlation by setting  $s = 0.53$  mag per 100 days in the peak magnitude–decay rate

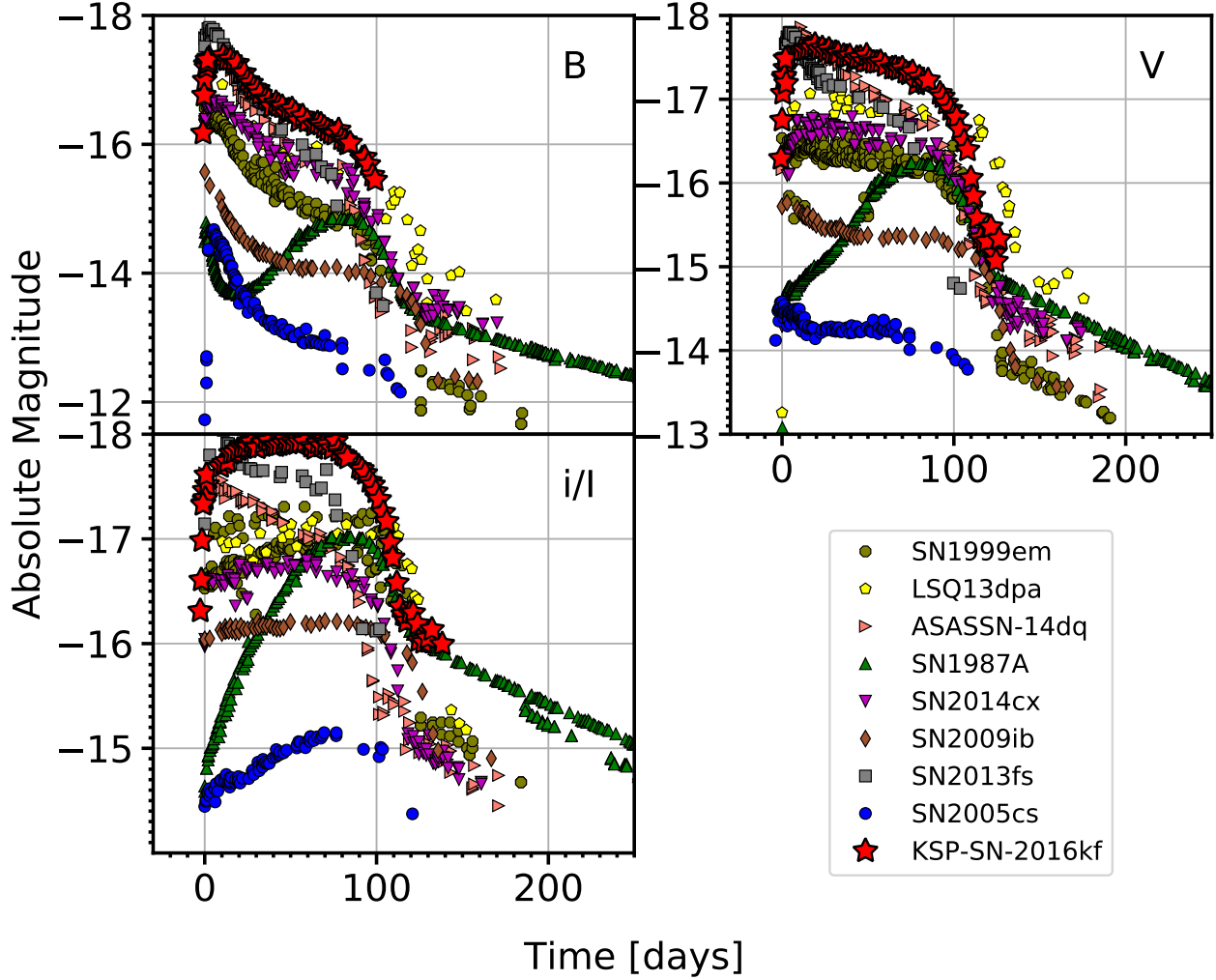


**Figure 4.** The light curve of KSP-SN-2016kf is compared against other well-observed or similar Type II SNe: SN1999em (Elmhamdi et al. 2003) LSQ13dpa (Valenti et al. 2016), ASASSN-14dq (Valenti et al. 2016), SN1987A (Hamuy et al. 1988), SN2014cx (Huang et al. 2016), SN2009ib (Takáts et al. 2015), SN2013fs (Yaron et al. 2017), and SN2005cs (Pastorello et al. 2009). Here, the light curves of KSP-SN-2016kf are binned into 1 day intervals to reduce the variance of the data points. The x-axis is time since  $B$ -band peak magnitude for each SNe (except for SN1987A which is presented relative to the first  $B$ -band detection). The shape of the light curves of KSP-SN-2016kf resembles than of SN2014cx, SN1999em, and LSQ13dpa, but is notably more luminous; in particular, KSP-SN-2016kf has the most luminous plateau (measured at 50 days) and tail luminosity in comparison with other Type II SNe shown here.

relation of Anderson et al. (2014). This gives the expected  $V$ -band peak magnitude of  $\sim -16.58$  mag which is  $\sim 1$  magnitude fainter than the observed  $V$ -band  $M_{\text{peak}} \approx -17.62$  mag presented in Table 3, indicating that KSP-SN-2016kf is not compatible with this correlation.

### 3.3. Color Analysis

Figure 5 (top panel) compares the  $B - V$  and  $V - i/I$  color evolution of KSP-SN-2016kf with those of a sample of other H-rich Type II SNe for the entire 130 days evolution, while Figure 5 (bottom panel) presents the same for the first 5 days of the evolution. Overall, the color evolution of KSP-SN-2016kf is similar to other shown SNe confirming its H-rich Type II nature. As in the Figure, the colors of these

SNe redden during the first  $\sim 50$  days in an almost linear manner, after which the color change rates become small before they enter the phase of the radioactive tail. While the color evolution of KSP-SN-2016kf is broadly similar to that of other prototypical H-rich Type II, KSP-SN-2016kf is redder than the other SNe, especially in  $B - V$  and during the first 5 days. The redder color of KSP-SN-2016kf does not appear to follow the correlations between the peak absolute magnitude and color in de Jaeger et al. (2018a). Based on this correlation, it is expected that fainter Type II SNe (in terms of peak absolute magnitude) will be redder in color, although it is worth noting that the dispersion on this correlation is quite large and as pointed by de Jaeger et al. (2018a) the intrinsic differences of the SN progenitors, including



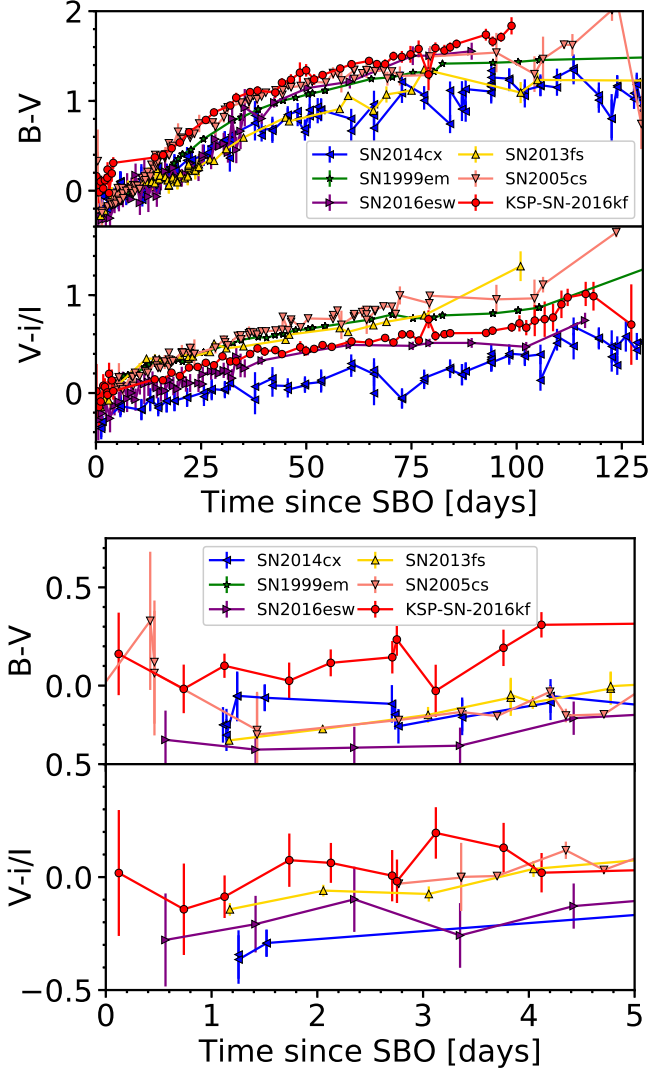


**Figure 5.** The color index of KSP-SN-2016kf along with other well-observed or similar Type II SNe: SN2014cx (Huang et al. 2016), SN1999em (Elmhamdi et al. 2003), SN2016esw (de Jaeger et al. 2018b), SN2013fs (Yaron et al. 2017), and SN2005cs (Pastorello et al. 2009). *Top:* the  $B - V$  and  $V - I$  of SNe are shown for less than 120 days since SBO. *Bottom:* the same as above but zoomed-in on the first week evolution.

progenitor radius and the CSM characteristics, are the contributing factors in the dispersion of the color. Note that the color of KSP-SN-2016kf’s radioactive tail is only shown in the  $V - I$  plot due to lack of  $t \gtrsim 100$  days data in  $B$  band. During the tail,  $V - I$  rapidly reddens by  $\sim 0.3$  mag over  $\sim 10$  days. A similar behaviour has been previously observed for other Type IIP SNe (e.g., SN2005cs; Pastorello et al. 2009).

### 3.4. Bolometric Light Curve and $^{56}\text{Ni}$ mass

Figure 6 shows the evolution of the bolometric luminosity (filled black circles) of KSP-SN-2016kf in comparison with that of SN1987A (red solid curve) as well as the relative decay

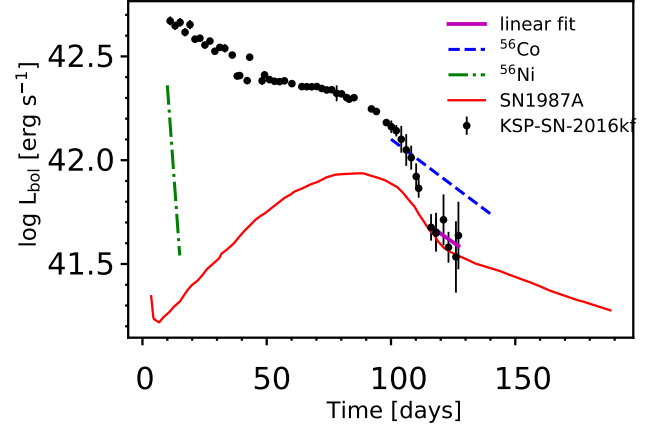


**Figure 6.** Bolometric light curve of KSP-SN-2016kf (black points) for which the absolute magnitudes are converted to bolometric luminosity by applying the bolometric correction of Lyman et al. (2014). For comparison, we also show the bolometric light curve of SN1987A from Suntzeff & Bouchet (1990) (red solid curve),  $^{56}\text{Co} \rightarrow ^{56}\text{Fe}$  decay rate (dashed blue curve), and  $^{56}\text{Ni} \rightarrow ^{56}\text{Co}$  decay rate (dash-dotted green curve). Note that the decay rates shown are relative and only represent the conversion slope of the radioactive chain. The magenta line shows a linear fit to the tail bolometric luminosity. We estimate  $M_{\text{Ni}} = 0.10 \pm 0.01 M_{\odot}$  from the tail luminosity of KSP-SN-2016kf.

rates of  $^{56}\text{Co} \rightarrow ^{56}\text{Fe}$  (dashed blue curve) and  $^{56}\text{Ni} \rightarrow ^{56}\text{Co}$  (dash-dotted green curve). In order to obtain bolometric luminosities of KSP-SN-2016kf, the absolute  $V$ -band magnitudes of KSP-SN-2016kf, shown in Figure 4, are converted to bolometric magnitudes using  $\text{BC} = M_{\text{bol}} - M_V$ , where BC is the bolometric correction (BC) of Lyman et al. (2014). In this formalism, BC is a color-dependent (here, we use  $V - I$  index) polynomial with coefficients listed in their Table 3 and 4. Finally, bolometric magnitudes are converted to luminosities assuming  $M_{\text{bol},\odot} = 4.74$  mag and  $L_{\text{bol},\odot} = 3.83 \times 10^{33}$  erg  $\text{s}^{-1}$ . Since the bolometric luminosity depends on  $V - I$  color evolution, our bolometric light curve is cut off at  $\sim 130$  days when KSP-SN-2016kf goes below the detection limit in  $V$  band.

The  $^{56}\text{Ni}$  mass ( $M_{\text{Ni}}$ ) synthesized in Type II SNe is often estimated by the tail bolometric luminosity, as the tail is dominantly powered by the  $^{56}\text{Ni} \rightarrow ^{56}\text{Co} \rightarrow ^{56}\text{Fe}$  radioactive decay chain. Figure 6 indicates that for  $t \gtrsim 115$  days the bolometric light curve of KSP-SN-2016kf transitions to a linearly declining radioactive tail which is  $\sim 25\%$  more luminous than that of SN1987A, implying a higher synthesized  $M_{\text{Ni}}$  based on the direct comparison of luminosities (See Equation 3 of Valenti et al. 2016). Following Appendix A of Valenti et al. (2008), we estimate  $M_{\text{Ni}} = 0.10 \pm 0.01 M_{\odot}$ , as presented in Table 2, using the known decay times of  $^{56}\text{Ni}$  and  $^{56}\text{Co}$  as well as their associated energy generation rates assuming the complete trapping of  $\gamma$ -rays and positrons

**Table 4.** Line velocities at epoch of 93 days

Line & Wavelength	Velocity [km s <sup>-1</sup> ]
H $\alpha$ $\lambda$ 6563	7960 $\pm$ 60
Fe II $\lambda$ 5169	3192 $\pm$ 63
Fe II $\lambda$ 5018	3134 $\pm$ 84
Fe II $\lambda$ 4924	2798 $\pm$ 55
H $\beta$ $\lambda$ 4861	5860 $\pm$ 45
H $\gamma$ $\lambda$ 4340	5452 $\pm$ 167
H $\delta$ $\lambda$ 4101	4818 $\pm$ 141

NOTE—The uncertainties are associated with the profile and continuum fitting method used for finding the minimum of the absorption features.

(supported by the similar slopes of the radioactive tail and  $^{56}\text{Co} \rightarrow ^{56}\text{Fe}$  decay rate, as shown in Figure 6).

#### 4. SPECTROSCOPY OF KSP-SN-2016kf

Figure 7 (top panel) compares the spectrum of KSP-SN-2016kf taken at an epoch of 93 days, which is near the transition from the plateau phase to the radioactive tail phase, with those of the other three well-observed H-rich Type II SNe at a similar phase. The spectrum of KSP-SN-2016kf exhibits prominent P-Cygni Balmer lines, classifying KSP-SN-2016kf as a Type II SN. Using the redshift of  $z = 0.043 \pm 0.002$  obtained from the host galaxy (see §5), the spectrum is redshifted to the rest frame.

In order to obtain the expansion velocities of KSP-SN-2016kf, we fit a Gaussian profile to the absorption feature of the P-Cygni profile of four Balmer lines of H $\alpha$ , H $\beta$ , H $\gamma$  and H $\delta$  as well as prominent iron lines, Fe II $\lambda$ 4924, Fe II $\lambda$ 5018, and Fe II $\lambda$ 5169 and measure the expansion velocity of each line at the minimum absorption of the fitted Gaussian profile. The measured expansion velocities, listed in Table 4, have a wide range of values; the H $\alpha$  has the highest velocity at  $\sim 7960$  km s<sup>-1</sup>, while Fe II $\lambda$ 4924 has the lowest velocity among the selected lines at  $\sim 2798$  km s<sup>-1</sup>. We can see that all Balmer lines have a higher expansion velocity than any of the three Fe II lines. This is because H lines are formed at much lower optical depths than Fe II lines, hence exhibit higher velocities. The velocities of Fe II $\lambda$ 5018 and Fe II $\lambda$ 5169 are often associated with the photospheric expansion velocity, as they are formed closer to the photosphere (Takáts & Vinkó 2012).

Although the spectrum of KSP-SN-2016kf in Figure 7 (top panel) is broadly similar to those of the other H-rich Type II SNe that we compare with, there are a few notable differences: (1) the H $\alpha$  line resembles that of SN2012aw, but broader (in both emission and absorption) with a shallower

absorption feature, (2) the H $\beta$  line appears much stronger than that of other SNe, producing a deep and broad absorption trough redwards of a prominent emission peak, which could be due to blending with other nearby lines, and (3) the Ba II line has a very small emission peak with no notable trough and is the weakest compared to that of other H-rich Type II SNe.

For constraining the metallicity of the SN progenitor, we measure the pseudo-Equivalent Width (pEW) of the absorption feature of Fe II $\lambda$ 5018 line. Recently, it has been shown that the pEW of this line during the plateau phase can probe the progenitor metallicity of H-rich Type II SNe. (Dessart et al. 2014; Taddia et al. 2016b; Gutiérrez et al. 2018). According to Figure 1 of Taddia et al. (2016b), pEW of Fe II $\lambda$ 5018 is correlated with the SN phase and metallicity. Our measured pEW of  $\sim 18$  Å at the epoch of 93 days corresponds to the metallicity of 0.1–0.4  $Z_{\odot}$ . This metallicity measurement complements the metallicity estimated based on several line diagnostics of the host galaxy spectrum (see §5)

#### 5. HOST GALAXY OF KSP-SN-2016kf

Figure 7 (bottom panel) shows the spectrum of the galaxy identified with “G” in Figure 1. The spectrum exhibits prominent Balmer H emission lines including H $\alpha$  and H $\beta$  as well as several other lines such as [O III]  $\lambda$ 3727, [O III]  $\lambda$ 4959, [O III]  $\lambda$ 5007, [N II]  $\lambda$ 6584, and [S II]  $\lambda$ 6717. The redshift of the galaxy, measured from the H $\alpha$  line, is  $z \approx 0.043$ , which is equivalent to the luminosity distance of 197.4 Mpc (see § 2.3). This redshift is consistent with that of KSP-SN-2016kf as shown in § 4, confirming that the galaxy is the host galaxy of the SN.

The host galaxy is 4'' (or  $\sim 3.4$  kpc at the angular diameter distance of 181.5 Mpc) away from the SN in the eastern direction. It has a small effective radius of  $\sim 2.2$  kpc (or  $\sim 2''5$ ). The galaxy is relatively bright with absolute magnitude of  $-17.57 \pm 0.06$  ( $B$ ),  $-18.17 \pm 0.08$  ( $V$ ), and  $-19.05 \pm 0.06$  ( $I$ ) mag for the size of the galaxy. Using the FAST stellar population synthesis code (Kriek et al. 2009) we find a best-fit stellar mass for the host galaxy of  $\log (M/M_{\odot}) = 8.73^{+0.51}_{-0.73}$ . These model calculations are based on the stellar library of Maraston (2005) and the assumption of exponential star formation history and Salpeter IMF.

The observed line intensity ratio between H $\alpha$  and H $\beta$  lines integrated over the host galaxy is  $3.11 \pm 0.26$  (Figure 7). Within the temperature range of 5000–20000 K, the intrinsic line intensity ratio of the two lines changes between 3.04 and 2.75 (Dopita & Sutherland 2003) for electron number density of 100 cm<sup>-3</sup>. By comparing the observed and intrinsic ratios, we obtain the extinction  $E(B - V)$  in the range of 0.02–0.10 mag (see Groves et al. 2012, and references therein), or  $A_V = 0.07$ –0.33 mag for  $R_V = 3.1$  using the extinction correction model by Fitzpatrick (1999). Con-

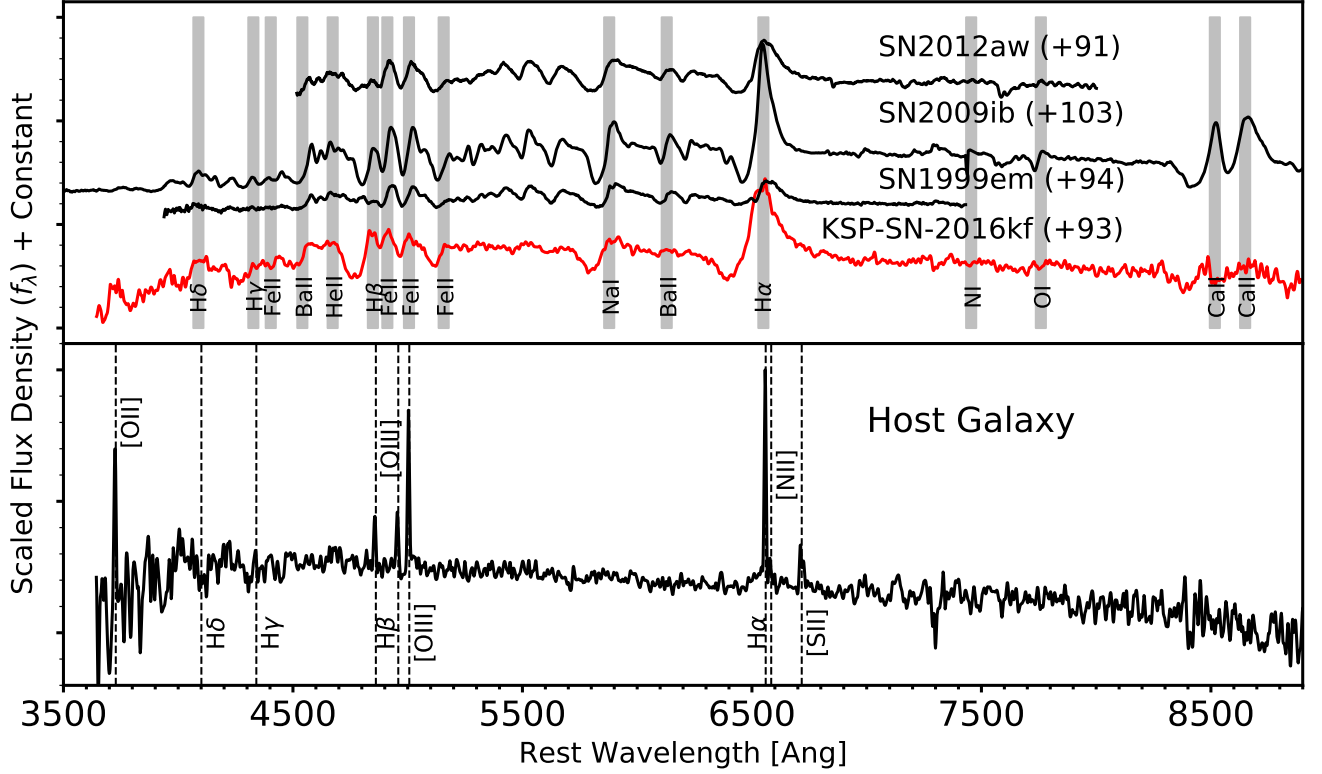


**Figure 7.** *Top:* Comparison of KSP-SN-2016kf (red curve) and other H-rich Type II SNe (black curves) at similar epochs. Note that the flux density for each SN is scaled by its distance squared for the fair comparison of features. The gray vertical lines indicate the wavelength of typical spectral lines visible at this epoch. *Bottom:* the spectrum of KSP-SN-2016kf’s host galaxy. The emission lines are marked with dashed lines.

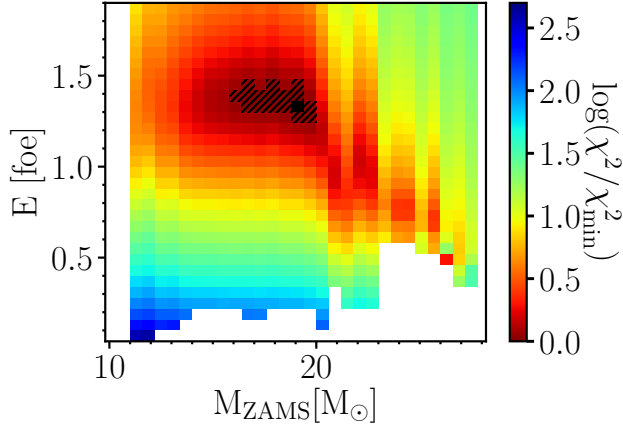


**Figure 8.** The scaled goodness of fit,  $\log(\chi^2 / \chi_{\min}^2)$ , where  $\chi_{\min} = 5100$  represents the goodness of fit for the best-fit model, for a grid of SNEC simulations with  $5 M_\odot$   $^{56}\text{Ni}$  mixing scheme and different ZAMS masses and explosion energies. The hatched squares represent best 2-percentile of fitted models. The best-fit model is marked with a filled black square and has  $\sim 18.8 M_\odot$  ZAMS mass,  $\sim 1.3$  foe explosion energy, and  $5 M_\odot$   $^{56}\text{Ni}$ . The evolved RSG progenitor of this model has  $M \approx 15 M_\odot$  and  $R \approx 1040 R_\odot$ .

sidering that KSP-SN-2016kf is located substantially away from the host galaxy (Figure 1), this small estimated extinc-

tion toward the center of the host galaxy is consistent with a negligible host-galaxy extinction toward the SN (see §2.3).

We find the metallicity of the host galaxy of KSP-SN-2016kf to be sub-solar, i.e.,  $Z/Z_\odot \approx 0.4$ , based on the analysis of the observed line ratios sensitive to O abundance and metallicity. For this estimate, we use O3N2 and N2 line ratio indicators (Marino et al. 2013) obtained with the observed fluxes of H, O and N lines in the host galaxy spectrum (Figure 7). The O3N2 and N2 indicators provide the O abundance of  $8.23 \pm 0.03$  and  $8.24 \pm 0.06$ , respectively, for the host galaxy, corresponding to  $Z/Z_\odot = 0.4 \pm 0.1$  assuming  $12 + \log(\text{O}/\text{H})_\odot = 8.69$  (Asplund et al. 2009). All abundances are calculated in PyMCZ code with the observed line fluxes (Bianco et al. 2016). The abundances from O3N2 and N2 line indicators are  $\sim 0.22$  and  $\sim 0.21$  dex, respectively, smaller than the median value of the O abundance found in other Type II SNe (Anderson et al. 2016). The  $Z/Z_\odot \approx 0.4$  host galaxy metallicity coincides with the upper bound value of the SN metallicity, i.e.,  $Z/Z_\odot \approx 0.1 - 0.4$  (§4). We note that this is consistent with the location of KSP-SN-2016kf in the outskirts of the host galaxy since the galaxy metallicity tends to drop from the center to outskirts (Taddia et al. 2015).

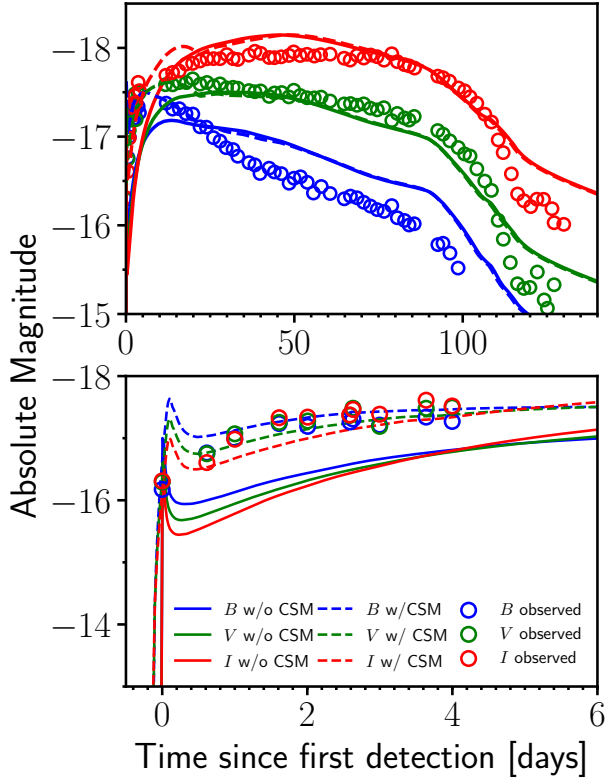


**Figure 9.** Comparison of the light curves for 1) the best-fit model without a CSM component (solid curves), 2) the best-fit model with a dense CSM component (dashed curves), and 3) observed values (open circles). *Top:* the observed and simulated light curves of KSP-SN-2016kf. *Bottom:* same as top panel but zoomed-in to show the early rise epochs.

### 6.1. Hydrodynamic Modelling

To constrain the physical parameters of KSP-SN-2016kf, we conduct the radiation transfer hydrodynamical simulations that give the best-fit parameters for the light curves. The simulations are carried out in open-source code SNEC (Morozova et al. 2015), a 1D flux-limited radiation transfer code which treats ionization levels and recombination under the local thermodynamic equilibrium (LTE) assumption. Similar to Morozova et al. (2018), we construct a grid of simulations with non-rotating RSG progenitor models in the ZAMS mass range of 11–28  $M_{\odot}$  with 0.6  $M_{\odot}$  resolution created by the KEPLER stellar evolution code (Woosley & Heger 2007). The explosion is launched by the thermal bomb mechanism and is evolved for 120 days, i.e., before the onset of the optically thin phase. We excise 1–2  $M_{\odot}$  at the center of the explosion to account for the mass of the proto-neutron SN remnant (Morozova et al. 2018). We adopt Paczynski (1983) equation of state implemented in SNEC for the RSG model and set the numerical grid size to 1000 cells in all of our simulations. In addition to varying the ZAMS mass of the KEPLER progenitor models, we also vary the

explosion energy in the range of 0.25–1.96 foe (where 1 foe =  $10^{51}$  erg  $s^{-1}$ ) with 0.06 foe resolution. For  $^{56}\text{Ni}$  mixing, we adopt three schemes for which the  $^{56}\text{Ni}$  is roughly mixed in the progenitor up until 3  $M_{\odot}$ , 5  $M_{\odot}$ , and 7  $M_{\odot}$  in mass coordinate within the progenitor. As described in §3.4, we fixed  $M_{\text{Ni}} = 0.10 M_{\odot}$  in the simulations.

The *BVI* light curves from SNEC simulations are then compared to the observed light curves by calculating  $\chi^2$  as below,

$$\chi^2 = \sum_{\lambda \in \{V, I\}} \sum_{t_{\text{SBO}} \leq t_* \leq 105} \frac{[M_{\text{obs}, \lambda}(t_*) - M_{\lambda}(t_*)]^2}{[\sigma_{\text{obs}, \lambda}(t_*)]^2}, \quad (2)$$

where  $\lambda$  denotes the corresponding band,  $t_*$  the time of observation,  $M_{\text{obs}, \lambda}$  the observed absolute magnitudes,  $M_{\lambda}$  the simulated absolute magnitudes, and  $\sigma_{\text{obs}, \lambda}$  the uncertainty of the observed magnitudes. We exclude the *B*-band light curve data due to the non-negligible effect of iron group line blanketing to the observed brightness (Dessart & Hillier 2010). We also exclude data from  $t_* > 105$  days because the LTE assumption may not hold for those epochs.

Figure 8 shows the normalized  $\chi^2$  by minimum  $\chi^2_{\text{min}}$  value from our SNEC simulations as a function of explosion energy ( $E$ ) and  $M_{\text{ZAMS}}$  for the case of 5  $M_{\odot}$   $^{56}\text{Ni}$  mixing. We found that 5  $M_{\odot}$   $^{56}\text{Ni}$  mixing scheme fits the observed light curves much better than the other two mixing schemes. The hatched squares represent best 2 percentile of best-fit models. The  $E$  and  $M_{\text{ZAMS}}$  of these models are, respectively, in the range of 1.24–1.4 foe and 15.8–19.4  $M_{\odot}$ , among which a model with 1.3 foe and 18.8  $M_{\odot}$  ZAMS mass best fits the observed light curves and is marked with a filled black square. The evolved RSG progenitor of this model has mass  $M \approx 15 M_{\odot}$  and radius  $R \approx 1040 R_{\odot}$ . Figure 9 compares the light curves of the best-fit model with the observed light curves of KSP-SN-2016kf. The model closely fits the observed values during the late time evolution (i.e.,  $t > 20$  days) in *V* and *I* bands, but during the early epochs the fits underestimate the luminosity of the observed light curve, probably due to the presence of CSM (see below).

### 6.2. Potential Interaction with Dense CSM

As shown in Figure 9, the comparison between the best-fit light curve and the observed light curves indicate the existence of additional emission in the early epochs. In order to understand the nature of this emission, we conducted additional SNEC simulations including a CSM component. We adopt a dense optically-thick, constant-velocity CSM with the density profile  $\rho(r) = K/r^2$  for  $r < R_{\text{CSM}}$  (e.g., Morozova et al. 2018) around the best-fit progenitor model described above. In the simulations, we vary the parameter  $K$  in the range of  $11 \times 10^{17} - 3 \times 10^{18}$  g  $\text{cm}^{-1}$  with resolution of  $10^{17}$  g  $\text{cm}^{-1}$  and  $R_{\text{CSM}}$  in the range 1040–3800  $R_{\odot}$  with reso-

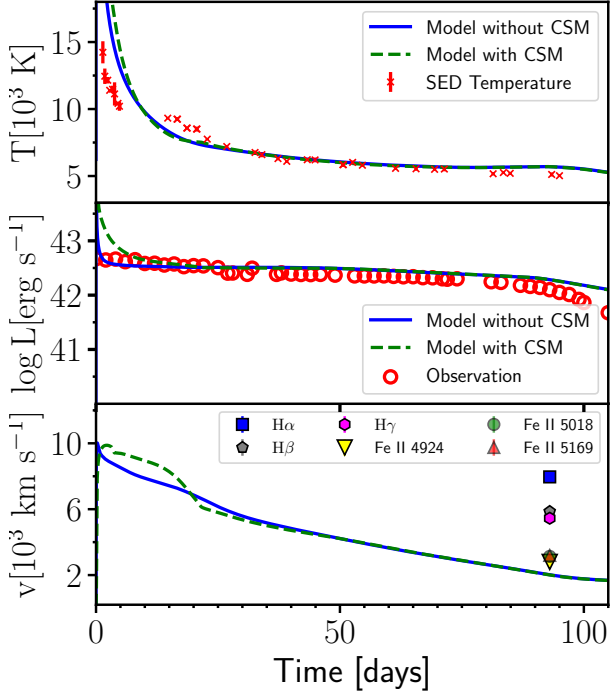


**Figure 10.** Blackbody temperature, bolometric luminosity, and photospheric velocity for the best-fit model without CSM component (solid blue curve) and with dense CSM component (dashed green curve) as well as the corresponding observationally estimated values. *Top*: photospheric temperature over time. Red open circles represent the blackbody temperature for the observed *BVI* magnitudes. *Middle*: bolometric light curve. The observed luminosities are shown with red open circles. *Bottom*: photospheric velocity. Several line velocities are also plotted.

lution  $100 R_{\odot}$ . We assume the composition and temperature of the CSM are equal to the outer part of a RSG with H fraction of 0.61, He fraction of 0.37, and temperature of 2400 K. The adoption of this type of dense optically-thick CSM is motivated by the increasing evidence of RSGs undergoing strong mass-loss shortly prior to the collapse of the core (see e.g., Khazov et al. 2016; Yaron et al. 2017; Hosseinzadeh et al. 2018; Bullivant et al. 2018; Forster et al. 2018).

We select the best-fit model with CSM component using Equation 2 in a similar manner as in §6.1 and find that a model with  $R_{\text{CSM}} \approx 1640 R_{\odot}$  and  $K \approx 4 \times 10^{17} \text{ g cm}^{-1}$  best matched observations. With these values of  $K$  and  $R_{\text{CSM}}$ , the total CSM mass between the progenitor and  $R_{\text{CSM}}$  is  $0.11 M_{\odot}$ , and this CSM mass along with the above  $K$  is equivalent to the mass loss rate of  $\sim 0.08 M_{\odot} \text{ yr}^{-1}$  assuming typical wind velocity of  $10 \text{ km s}^{-1}$ . The SNEC simulations also provide information for the SBO, which occurs inside the CSM near its outer edge at radius  $\sim 1550 R_{\odot}$  or optical depth  $\tau \approx 95$ . Figure 9 also shows the light curves of the best-fit model with the CSM component along with the best-fit model without the CSM component. As in the figure, the

model that includes the CSM component fits the observed early light curves significantly better than the best-fit model without it.

Figure 10 compares observationally estimated blackbody temperatures (top panel) and bolometric luminosities (middle panel) with those of the best-fit models, both with and without the CSM component. The temperatures represent best-fit black body temperatures from the observed *BVI* magnitudes, while the observed bolometric luminosity is calculated after applying proper bolometric corrections (§3.4). The modelled bolometric luminosity is measured at the photosphere. Figure 10 (bottom panel) also compares velocities of several spectral lines at the epoch of 93 days (presented in Table 4) and the simulated photospheric velocities.

As seen in Figure 10, the temperature and luminosity derived from observations match well with those from the best-fit model during the later epoch. There are, however, slight discrepancies in temperature and luminosity during the early ( $t \lesssim 5$  days) epoch: (1) in temperature, the models (both with and without CSM) predict higher (by 2500 K) temperature than the observations; (2) in luminosity; while the observations match the predictions from the model without the CSM component, the model with CSM overpredicts the observed luminosity. The discrepancy (1) can be due to inaccurate temperatures estimated from *BVI* light curves as the temperature is high and the observed bands do not cover the peak SED intensity or potential deviation from a blackbody spectrum in the presence of CSM (Chevalier & Irwin 2011), while the apparent discrepancy in (2) may arise from inaccurate bolometric correction for the early envelope cooling phase for SNe with CSM. These overall agreement in temperature and luminosity, together with the similarity in the photospheric velocities of the model and Fe II line velocities—which is associated with the photospheric velocity as discussed by §4—indicate that the observed light curves of KSP-SN-2016kf are reasonably well-reproduced in our simulations.

It is worth noting that our estimates on the  $K$  and  $R_{\text{CSM}}$  of the potential dense CSM component should be regarded as a lower limit due to the LTE assumption in SNEC. It is likely that this assumption breaks down when the shock moves into the CSM, in which case the temperature of the photons would significantly exceed that calculated in the simulations under the LTE assumption. This leads to a longer rise time as it takes more time for the color temperature (i.e., spectrum peak) to drop into the observed band (Nakar & Sari 2010).

## 7. DISCUSSION

KSP-SN-2016kf is a H-rich Type II SN with a long rise time ( $t_{\text{rise}} \approx 19.9$  days in *V* band), a relatively luminous peak ( $M_V \approx -17.62$  mag), a highly luminous plateau ( $M_V \approx$

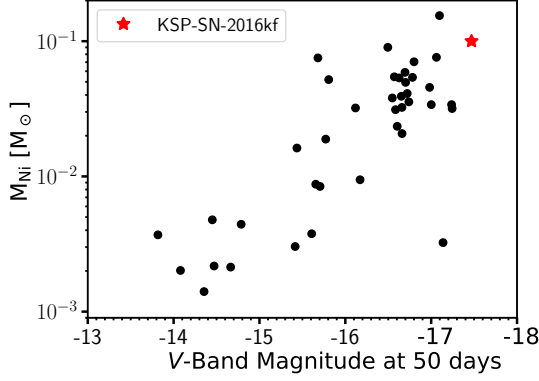


**Figure 11.**  $^{56}\text{Ni}$  mass and plateau magnitude at the epoch of 50 days for a sample of Type II SNe in Valenti et al. (2016). The red star represents KSP-SN-2016kf which is located at higher end of both  $^{56}\text{Ni}$  mass and plateau magnitude.

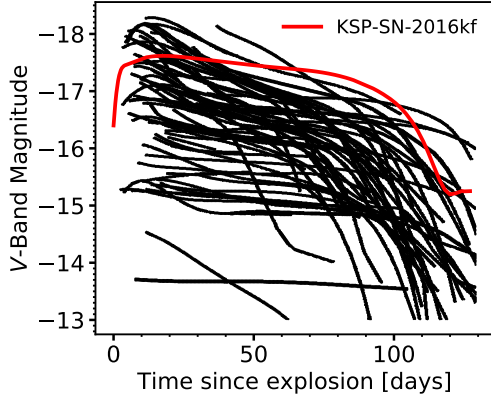


**Figure 12.** Comparison of the V-band light curve of KSP-SN-2016kf (red curve) and that of other Type II SNe in Anderson et al. (2014). The light curve of KSP-SN-2016kf is comparatively flat and luminous during the plateau phase.

–17.47 mag at the epoch of 50 days), and a low decay rate ( $s \approx 0.53$  mag per 100 days). Its tail part ( $t \gtrsim 105$  days) is exceptionally bright, requiring a large  $^{56}\text{Ni}$  mass of  $\sim 0.1 M_{\odot}$  to power the tail luminosity. The SN likely resulted from an explosion with  $\sim 1.3$  foe energy in a RSG, evolved from a  $\sim 18.8 M_{\odot}$  ZAMS mass, whose mass and radius are  $\sim 15 M_{\odot}$  and  $\sim 1040 R_{\odot}$ , respectively, at the time of explosion. The early light curves of KSP-SN-2016kf indicate the presence of CSM.

Figure 11 compares the  $^{56}\text{Ni}$  mass and the plateau magnitude of KSP-SN-2016kf at the epoch of 50 days to those of most other Type II SNe at the same epoch presented in Valenti et al. (2016), showing a positive correlation between two parameters. This correlation has been also reported in several previous studies (Hamuy 2003; Spiro et al. 2014;

Pejcha & Prieto 2015; Valenti et al. 2016). KSP-SN-2016kf appears to have the most luminous plateau among the shown sample of Type II SNe as well as one of the highest inferred  $^{56}\text{Ni}$  masses, while it still follows the known correlation. The  $^{56}\text{Ni}$  mass of Type II SNe has also been known to be correlated with the explosion energy (Hamuy 2003; Pejcha & Thompson 2015; Müller et al. 2017), and the  $^{56}\text{Ni}$  mass of  $\sim 0.1 M_{\odot}$  and 1.3 foe explosion energy of KSP-SN-2016kf appear to follow the correlations in those studies.

Figure 12 shows the V-band light curves of a sample of Type II SNe presented in Anderson et al. (2014) in comparison with that of KSP-SN-2016kf. We can easily identify that the plateau of KSP-SN-2016kf is flatter than those of other SNe with comparable luminosity. The known correlation between the high peak luminosity and the plateau decay rate (Anderson et al. 2014) predicts much higher decay rate than what we observed for KSP-SN-2016kf. Since we estimated a large amount of  $^{56}\text{Ni}$ , its flatter plateau may indicate the presence of an early contribution of the  $^{56}\text{Ni}$  radioactive decay to the plateau luminosity (Nakar et al. 2016).

As in Figure 11, KSP-SN-2016kf has one of the largest  $M_{\text{Ni}}$  among the sample of Valenti et al. (2016). This is also consistent with the sample of 19 H-rich Type IIP SNe in Müller et al. (2017), whose median  $M_{\text{Ni}}$  is  $0.031 M_{\odot}$ . High  $^{56}\text{Ni}$  masses in the range of  $0.1$ – $1.6 M_{\odot}$  have been previously reported for several Type II SNe including SN1992H (Hamuy 2003), SN1992af (Valenti et al. 2016), SN1992am (Hamuy 2003), SN 2016ija (Tartaglia et al. 2018), and ASASSN-15nx (Bose et al. 2018), although there are large uncertainties associated with the inferred large  $M_{\text{Ni}}$  of some of these SNe due to possible alternative power sources at later epochs, unknown dust extinction, and limited photometric data over the light curve tail.

It appears that the observationally estimated  $^{56}\text{Ni}$  mass of a group of SNe, including those mentioned above, is higher than the typical  $M_{\text{Ni}}$  upper limit of  $\sim 0.12 M_{\odot}$  predicted by neutrino-driven CCSN simulations (e.g., Ugliano et al. 2012; Pejcha & Thompson 2015; Sukhbold et al. 2016). Therefore, it is important to increase the sample size of SNe with large  $^{56}\text{Ni}$  mass to draw firm conclusions on the compatibility of neutrino-driven CCSN simulations and the observations in terms of  $^{56}\text{Ni}$  mass production. For KSP-SN-2016kf, our estimated  $M_{\text{Ni}} \approx 0.1 M_{\odot}$  is within the predicted  $M_{\text{Ni}}$  range of  $0.003$ – $0.12 M_{\odot}$  for the successful SN explosions in the neutrino-driven CCSN simulations of Sukhbold et al. (2016) and our obtained explosion energy of 1.3 foe is compatible with the production of the  $0.1 M_{\odot}$  of  $^{56}\text{Ni}$  based on the positive correlation between two parameters (Sukhbold et al. 2016, see their Figure 17).

The large ZAMS mass,  $\sim 18.8 M_{\odot}$  (Section 6), of the progenitor of KSP-SN-2016kf provides an important insight into how H-rich Type II SNe explode. According to Smartt et al.

(2009), large RSGs, whose mass during their ZAMS phase were greater than  $\sim 17 M_{\odot}$ , have been very rare as progenitors of Type II SNe. This lack of RSG progenitors with a large ZAMS mass, known as the ‘‘RSG problem’’, appears to be consistent with what is predicted by numerical simulations of neutrino-driven CCSNe which substantially favor ZAMS stars of smaller mass,  $\lesssim 17 M_{\odot}$ , as the progenitor of Type II SNe (Ugliano et al. 2012; O’Connor & Ott 2013; Sukhbold et al. 2016). In this scenario, ZAMS stars of mass  $\gtrsim 17 M_{\odot}$  tend to directly implode to a BH or produce failed SNe without SN-like activity. The recent discovery of a large mass RSG progenitor with metallicity of  $\sim 0.1$  (Anderson et al. 2016) shows that metallicity may play an important role, although it is difficult to reach a firm conclusion due to the lack of other observational examples supporting the idea. KSP-SN-2016kf appears to support the interpretation that a link between low metallicity progenitors and SN in massive RSGs may exist.

The light curves of KSP-SN-2016kf indicate the presence of a CSM component similar to the one assumed in Morozova et al. (2018). However, recent numerical simulations including wind acceleration predict a CSM component that is more extended and less massive than what is required in KSP-SN-2016kf. This emphasizes the need to obtain early spectra that can constrain the properties of CSM more rigorously.

Finally, we note that our results of the progenitor parameters of KSP-SN-2016kf are based on model calculations relying on three key assumptions: (1) the SN explosion is spherical; hence, a 1D model is sufficient; (2) the LTE assumption holds for the first 105 days since the explosion; and (3) non-rotating pre-SN models are adequate for the progenitor. Although these assumptions have been commonly adopted in similar studies of Type II SNe in practice, the results based on these assumptions should be taken with caution in principle since we cannot rule out the possibility that the real situations are in fact much different from the assumptions. The first assumption on the sphericity of the SN progenitor and explosion is motivated by the fact that developing significant asymmetries and non-radial flows in RSGs is much more difficult than in compact stripped-envelope progenitors and requires extreme aspherical explosions or oblate progenitors (Matzner et al. 2013, e.g.). Similarly, the LTE assumption is relevant for RSG progenitors as the post-SN RSG shock propagates slowly enough for the shocked material to generate sufficient photons for maintaining the equilibrium (Nakar & Sari 2010), although departure from LTE may happen considering CSM interaction as discussed in §6.2. For the third assumption on non-rotating RSG models, it is important to note that fast rotation may cause the H envelope of the stars in the initial mass range of  $15\text{--}20 M_{\odot}$  to be removed due to changes in core structure and enhanced

mass loss, leading to Type IIb or Ib/c SNe rather than Type II SNe (Hirschi et al. 2004). It is, therefore, more difficult for rapidly-rotating and massive RSGs to explode as a Type II SN.

## 8. SUMMARY AND CONCLUSION

In this paper, we present the photometric, and spectroscopic analyses of KSP-SN-2016kf and its host galaxy discovered by KMTNet. Our multi-color high-cadence observations of KSP-SN-2016kf give a tight constraint on the shock breakout epoch as well as reliable estimates of its rise times. Based on a comprehensive modelling of the observed properties and also comparison with other Type II SNe, we summarize the properties and peculiarities of KSP-SN-2016kf as follows:

- (1) KSP-SN-2016kf has an exceptionally long rise time for a H-rich Type II SN, particularly among high luminosity ones, with  $t_{\text{rise}} \simeq 20$  and  $\simeq 50$  days in  $V$  and  $I$  bands, respectively.
- (2) The light curves of KSP-SN-2016kf have a moderately bright peak with  $M_V \simeq -17.6$  mag, but highly luminous plateau with  $M_V \simeq -17.4$  mag at 50 days. The plateau is one of the most luminous ones ever observed for H-rich Type II SNe.
- (3) KSP-SN-2016kf also has an exceptionally luminous radioactive tail, requiring  $0.10 \pm 0.01 M_{\odot}$  of  $^{56}\text{Ni}$  mass to power the radioactive tail of the light curves.
- (4) The plateau phase of the light curves shows  $\sim 0.53$  mag per 100 days decay rate in  $V$  band, which is smaller than what is expected from the known decay rate–peak luminosity correlation (Anderson et al. 2014). This may indicate the early contribution of  $^{56}\text{Ni}$  radioactive decay to the luminosity as discussed by Nakar et al. (2016).
- (5) From modelling of the light curves, the best-fit progenitor is a  $\sim 18.8 M_{\odot}$  ZAMS star that evolved into mass of  $\sim 15 M_{\odot}$  and radius of  $\sim 1040 R_{\odot}$  before an explosion of  $\sim 1.3$  foe.
- (6) The KSP-SN-2016kf appears to have subsolar metallicity with  $Z/Z_{\odot} \simeq 0.1 - 0.4$ .
- (7) Comparison between the observed light curves and modelled light curves of KSP-SN-2016kf indicate that a CSM component may have been present around its progenitor.
- (8) The production of  $0.10 \pm 0.01 M_{\odot}$  of  $^{56}\text{Ni}$  mass in an explosion of  $\sim 1.3$  foe is consistent with the predictions of the neutrino-derived CCSN simulations of Sukhbold et al. (2016).
- (9) The estimated ZAMS mass of  $\sim 18.8 M_{\odot}$  for KSP-SN-2016kf progenitor is higher than the range of  $M_{\text{ZAMS}} \lesssim 17 M_{\odot}$  obtained for the RSG progenitor of observed Type II SNe (see e.g., Smartt et al. 2009, for the RSG problem).
- (10) The large ZAMS mass of KSP-SN-2016kf together with its subsolar metallicity is suggestive of a potential link be-

tween low metallicity progenitors and SN in massive RSGs (Anderson et al. 2018).

This research has made use of the KMTNet facility operated by the Korea Astronomy and Space Science Institute and the data were obtained at three host sites of CTIO in Chile, SAAO in South Africa, and SSO in Australia. We acknowledge with thanks the variable star observations from the AAVSO International Database contributed by observers worldwide and used in this research. Our simulations were carried out on Compute Canada resources. PyRAF is product of the Space Telescope Science Institute, which is operated by AURA for NASA. N.A. was supported by QEII-GSST and OGS Fellowships. D.S.M. was supported in part by a Leading Edge Fund from the Canadian Foundation for Innovation (project No. 30951) and a Discovery Grant from the Natural Sciences and Engineering Research Council of Canada. Support for this work was provided to M.R.D. by NASA through Hubble Fellowship grant NSG-HF2-51373 awarded by the Space Telescope Science Institute, which is operated by the Association of Universities

for Research in Astronomy, Inc., for NASA, under contract NAS5-26555. M.R.D. acknowledges support from the Dunlap Institute at the University of Toronto. SGG acknowledges the support from the Portuguese Strategic Programme UID/FIS/00099/2013 for CENTRA and the FCT project PTDC/FIS-AST/31546/2017. Support for G.P. is provided by the Ministry of Economy, Development, and Tourism's Millennium Science Initiative through grant IC120009, awarded to The Millennium Institute of Astrophysics, MAS. Finally, we thank the anonymous referee for helpful comments on the original draft of this work.

*Software:* SNEC (Morozova et al. 2015), NumPy (van der Walt et al. 2011), Matplotlib (Hunter 2007), Astropy (Astropy Collaboration et al. 2013, 2018), FAST (Kriek et al. 2009), Hotpants (Becker 2015), IRAF (Tody 1993), SCAMP (Bertin 2006), SWARP (Bertin et al. 2002), PyMCZ (Bianco et al. 2016), KEPLER (Woosley & Heger 2007), ds9 (Joye & Mandel 2003), PyRAF

*Facility:* KMTNet, DuPont, SciNet, AAVSO

## REFERENCES

- Adams, S. M., Kochanek, C. S., Gerke, J. R., Stanek, K. Z., & Dai, X. 2017, *MNRAS*, 468, 4968
- Afsariadchi, N., & Matzner, C. D. 2018, *ApJ*, 856, 146
- Anderson, J. P., González-Gaitán, S., Hamuy, M., et al. 2014, *ApJ*, 786, 67
- Anderson, J. P., Gutiérrez, C. P., Dessart, L., et al. 2016, *A&A*, 589, A110
- Anderson, J. P., Dessart, L., Gutiérrez, C. P., et al. 2018, *Nature Astronomy*, 2, 574
- Antoniadis, J., Moon, D.-S., Ni, Y. Q., et al. 2017, *ApJ*, 844, 160
- Arcavi, I. 2017, *Hydrogen-Rich Core-Collapse Supernovae*, ed. A. W. Alsabti & P. Murdin, 239
- Arcavi, I., Gal-Yam, A., Cenko, S. B., et al. 2012, *ApJL*, 756, L30
- Asplund, M., Grevesse, N., Sauval, A. J., & Scott, P. 2009, *ARA&A*, 47, 481
- Astropy Collaboration, Robitaille, T. P., Tollerud, E. J., et al. 2013, *A&A*, 558, A33
- Astropy Collaboration, Price-Whelan, A. M., Sipócz, B. M., et al. 2018, *AJ*, 156, 123
- Bazin, G., Palanque-Delabrouille, N., Rich, J., et al. 2009, *A&A*, 499, 653
- Becker, A. 2015, *HOTPANTS: High Order Transform of PSF AND Template Subtraction*, *Astrophysics Source Code Library*, ascl:1504.004
- Bertin, E. 2006, in *Astronomical Society of the Pacific Conference Series*, Vol. 351, *Astronomical Data Analysis Software and Systems XV*, ed. C. Gabriel, C. Arviset, D. Ponz, & S. Enrique, 112
- Bertin, E., Mellier, Y., Radovich, M., et al. 2002, in *Astronomical Society of the Pacific Conference Series*, Vol. 281, *Astronomical Data Analysis Software and Systems XI*, ed. D. A. Bohlender, D. Durand, & T. H. Handley, 228
- Bianco, F. B., Modjaz, M., Oh, S. M., et al. 2016, *Astronomy and Computing*, 16, 54
- Blondin, S., Matheson, T., Kirshner, R. P., et al. 2012, *AJ*, 143, 126
- Bose, S., Dong, S., Kochanek, C. S., et al. 2018, *ArXiv e-prints*, arXiv:1804.00025
- Brown, S., Moon, D.-S., Ni, Y. Q., et al. 2018, *ApJ*, 860, 21
- Bullivant, C., Smith, N., Williams, G. G., et al. 2018, *MNRAS*, 476, 1497
- Chevalier, R. A., & Irwin, C. M. 2011, *ApJL*, 729, L6
- Davies, B., & Beasor, E. R. 2018, *MNRAS*, 474, 2116
- de Jaeger, T., Anderson, J. P., Galbany, L., et al. 2018a, *MNRAS*, 476, 4592
- de Jaeger, T., Galbany, L., Gutiérrez, C. P., et al. 2018b, *MNRAS*, 478, 3776
- Dessart, L., & Hillier, D. J. 2010, *MNRAS*, 405, 2141
- Dessart, L., Gutierrez, C. P., Hamuy, M., et al. 2014, *MNRAS*, 440, 1856
- Dopita, M. A., & Sutherland, R. S. 2003, *Astrophysics of the diffuse universe*
- Drout, M. R., Soderberg, A. M., Gal-Yam, A., et al. 2011, *ApJ*, 741, 97
- Elmhamdi, A., Danziger, I. J., Chugai, N., et al. 2003, *MNRAS*, 338, 939
- Fitzpatrick, E. L. 1999, *PASP*, 111, 63



- Forster, F., Moriya, T. J., Maureira, J. C., et al. 2018, *Nature Astronomy*, 2, 808
- Fuller, J. 2017, *MNRAS*, 470, 1642
- Fuller, J., & Ro, S. 2018, *MNRAS*, 476, 1853
- Gal-Yam, A., Arcavi, I., Ofek, E. O., et al. 2014, *Nature*, 509, 471
- González-Gaitán, S., Tominaga, N., Molina, J., et al. 2015, *MNRAS*, 451, 2212
- Groves, B., Brinchmann, J., & Walcher, C. J. 2012, *MNRAS*, 419, 1402
- Gutiérrez, C. P., Anderson, J. P., Sullivan, M., et al. 2018, *MNRAS*, 479, 3232
- Hamuy, M. 2003, *ApJ*, 582, 905
- Hamuy, M., Suntzeff, N. B., Gonzalez, R., & Martin, G. 1988, *AJ*, 95, 63
- He, M. Y., Moon, D.-S., Neilson, H., et al. 2016, *Journal of Korean Astronomical Society*, 49, 209
- Hirschi, R., Meynet, G., & Maeder, A. 2004, *A&A*, 425, 649
- Hosseinzadeh, G., Valenti, S., McCully, C., et al. 2018, *ApJ*, 861, 63
- Huang, F., Wang, X., Zampieri, L., et al. 2016, *ApJ*, 832, 139
- Hunter, J. D. 2007, *Computing in Science and Engineering*, 9, 90
- Joye, W. A., & Mandel, E. 2003, in *Astronomical Society of the Pacific Conference Series*, Vol. 295, *Astronomical Data Analysis Software and Systems XII*, ed. H. E. Payne, R. I. Jedrzejewski, & R. N. Hook, 489
- Kasen, D. 2010, *ApJ*, 708, 1025
- Khazov, D., Yaron, O., Gal-Yam, A., et al. 2016, *ApJ*, 818, 3
- Kim, S.-L., Lee, C.-U., Park, B.-G., et al. 2016, *Journal of Korean Astronomical Society*, 49, 37
- Kriek, M., van Dokkum, P. G., Labbé, I., et al. 2009, *ApJ*, 700, 221
- Lasker, B. M., Lattanzi, M. G., McLean, B. J., et al. 2008, *AJ*, 136, 735
- Lee, Y., Park, H. S., Kim, S. C., et al. 2018, *ApJ*, 859, 5
- Levesque, E. M., Massey, P., Olsen, K. A. G., et al. 2005, *ApJ*, 628, 973
- . 2006, *ApJ*, 645, 1102
- Lyman, J. D., Bersier, D., & James, P. A. 2014, *MNRAS*, 437, 3848
- Lyman, J. D., Bersier, D., James, P. A., et al. 2016, *MNRAS*, 457, 328
- Maraston, C. 2005, *MNRAS*, 362, 799
- Marino, R. A., Rosales-Ortega, F. F., Sánchez, S. F., et al. 2013, *A&A*, 559, A114
- Matheson, T., Kirshner, R. P., Challis, P., et al. 2008, *AJ*, 135, 1598
- Matzner, C. D., Levin, Y., & Ro, S. 2013, *ApJ*, 779, 60
- Matzner, C. D., & McKee, C. F. 1999, *ApJ*, 510, 379
- Moon, D.-S., Kim, S. C., Lee, J.-J., et al. 2016, in *Proc. SPIE*, Vol. 9906, *Ground-based and Airborne Telescopes VI*, 99064I
- Morozova, V., Piro, A. L., Renzo, M., et al. 2015, *ApJ*, 814, 63
- Morozova, V., Piro, A. L., & Valenti, S. 2018, *ApJ*, 858, 15
- Müller, T., Prieto, J. L., Pejcha, O., & Clocchiatti, A. 2017, *ApJ*, 841, 127
- Nakar, E., & Sari, R. 2010, *ApJ*, 725, 904
- Nakar, E., Poznanski, D., & Katz, B. 2016, *ApJ*, 823, 127
- O'Connor, E., & Ott, C. D. 2013, *ApJ*, 762, 126
- Oke, J. B., & Sandage, A. 1968, *ApJ*, 154, 21
- Paczynski, B. 1983, *ApJ*, 267, 315
- Park, H. S., Moon, D.-S., Zaritsky, D., et al. 2017, *ApJ*, 848, 19
- Pastorello, A., Valenti, S., Zampieri, L., et al. 2009, *MNRAS*, 394, 2266
- Pejcha, O., & Prieto, J. L. 2015, *ApJ*, 806, 225
- Pejcha, O., & Thompson, T. A. 2015, *ApJ*, 801, 90
- Planck Collaboration, Aghanim, N., Akrami, Y., et al. 2018, *ArXiv e-prints*, arXiv:1807.06209
- Popov, D. V. 1993, *ApJ*, 414, 712
- Poznanski, D., Prochaska, J. X., & Bloom, J. S. 2012, *MNRAS*, 426, 1465
- Quataert, E., & Shiode, J. 2012, *MNRAS*, 423, L92
- Rabinak, I., & Waxman, E. 2011, *ApJ*, 728, 63
- Ro, S., & Matzner, C. D. 2017, *ApJ*, 841, 9
- Rubin, A., & Gal-Yam, A. 2017, *ApJ*, 848, 8
- Rubin, A., Gal-Yam, A., De Cia, A., et al. 2016, *ApJ*, 820, 33
- Sanders, N. E., Soderberg, A. M., Gezari, S., et al. 2015, *ApJ*, 799, 208
- Schlafly, E. F., & Finkbeiner, D. P. 2011, *ApJ*, 737, 103
- Smartt, S. J. 2009, *ARA&A*, 47, 63
- . 2015, *PASA*, 32, e016
- Smartt, S. J., Eldridge, J. J., Crockett, R. M., & Maund, J. R. 2009, *MNRAS*, 395, 1409
- Smith, N. 2014, *ARA&A*, 52, 487
- Spiro, S., Pastorello, A., Pumo, M. L., et al. 2014, *MNRAS*, 439, 2873
- Sukhbold, T., Ertl, T., Woosley, S. E., Brown, J. M., & Janka, H.-T. 2016, *ApJ*, 821, 38
- Suntzeff, N. B., & Bouchet, P. 1990, *AJ*, 99, 650
- Taddia, E., Sollerman, J., Fremling, C., et al. 2015, *A&A*, 580, A131
- . 2016a, *ArXiv e-prints*, arXiv:1601.07368
- Taddia, E., Moquist, P., Sollerman, J., et al. 2016b, *A&A*, 587, L7
- Takáts, K., & Vinkó, J. 2012, *MNRAS*, 419, 2783
- Takáts, K., Pignata, G., Pumo, M. L., et al. 2015, *MNRAS*, 450, 3137
- Tartaglia, L., Sand, D. J., Valenti, S., et al. 2018, *ApJ*, 853, 62
- Tody, D. 1993, in *Astronomical Society of the Pacific Conference Series*, Vol. 52, *Astronomical Data Analysis Software and Systems II*, ed. R. J. Hanisch, R. J. V. Brissenden, & J. Barnes, 173
- Ugliano, M., Janka, H.-T., Marek, A., & Arcones, A. 2012, *ApJ*, 757, 69
- Valenti, S., Benetti, S., Cappellaro, E., et al. 2008, *MNRAS*, 383, 1485
- Valenti, S., Howell, D. A., Stritzinger, M. D., et al. 2016, *MNRAS*, 459, 3939
- van der Walt, S., Colbert, S. C., & Varoquaux, G. 2011, *Computing in Science and Engineering*, 13, 22
- van Loon, J. T., Cioni, M. R. L., Zijlstra, A. A., & Loup, C. 2005, *A&A*, 438, 273
- Walmswell, J. J., & Eldridge, J. J. 2012, *MNRAS*, 419, 2054
- Woosley, S. E., & Heger, A. 2007, *PhR*, 442, 269

Yaron, O., Perley, D. A., Gal-Yam, A., et al. 2017, *Nature Physics*, 13, 510